Quantitative visualization of swirl and cloud bubbles in Taylor–Couette flow

Bruno van Ruymbeke, Yuichi Murai, Yuji Tasaka, Yoshihiko Oishi, Céline Gabillet, Catherine Colin, Noureddine Latrache

**Bruno van Ruymbeke · Yuichi Murai · Yuji Tasaka · Yoshihiko Oishi · Céline Gabillet ·
Catherine Colin · Noureddine Latrache**

Quantitative visualization of swirl and cloud bubbles in Taylor–Couette flow

Abstract We develop a novel method to study the gas phase features in a bubbly Taylor–Couette flow when bubbles are arranged as elevated toroidal strings. The flow is recorded in the front view plane with a high-speed camera for a Reynolds number of 1500 and a global void fraction of 0.14 %. An image processing algorithm is developed to discriminate bubbles accumulated in clouds near the inner cylinder (cloud bub-bles) from bubbles trapped in the bulk flow by vortices (swirl bubbles). The analysis of the preferential positions, azimuthal velocities, and equivalent void fraction of clouds and swirl bubbles separately provides a new insight into the dynamics of the bubble's entrapment.

Keywords Bubbly Taylor–Couette · Flow visualization · Algorithm · Discrimination

1 Introduction

In the context of naval hydrodynamics, injecting bubbles into the developing boundary layer along the hull of ships can significantly reduce the frictional resistance by interacting with the near-wall turbulent structures (Kumagai et al. 2015). The Taylor–Couette (TC) flow that consists of a flow confined in the gap between two coaxial differentially rotating cylinders is considered an academic platform to investigate the drag reduction by injecting bubbles. When the outer cylinder is at rest, the occurrence of Taylor vortices and the array of toroidal vortices accompanied by inflow/outflow jets play the same role as sweeps and ejections of turbulent boundary layers with regard to the bubbles. Generally speaking, bubbles are arranged as axially periodic toroidal patterns: they can be trapped in the outflow region near the inner cylinder between the clockwise (CW) and counter-clockwise vortices (CCW) and inside the core of these two vortices (Yoshida et al. 2009, Fig. 1a). This arrangement of bubbles is known as *triple capture*.

Climent et al. (2007) investigated numerically the preferential location of bubbles in the wavy vortex flow (WVF) regime, where the Taylor vortices take azimuthal waves. Their results showed preferential

B. van Ruymbeke (✉) · C. Gabillet
IRENav, EA3634 French Naval Academy, Brest, France
E mail: bruno.van ruymbeke@ecole navale.fr
Tel.: +33 (0)2 98 23 43 06

Y. Murai · Y. Tasaka · Y. Oishi
Graduate School of Engineering, Hokkaido University, Kita 13, Nishi 8, Kita ku, Sapporo, Japan

C. Colin
IMFT, UMR 5502 CNRS/INP ENSEEIHT/UPS, Toulouse, France

N. Latrache
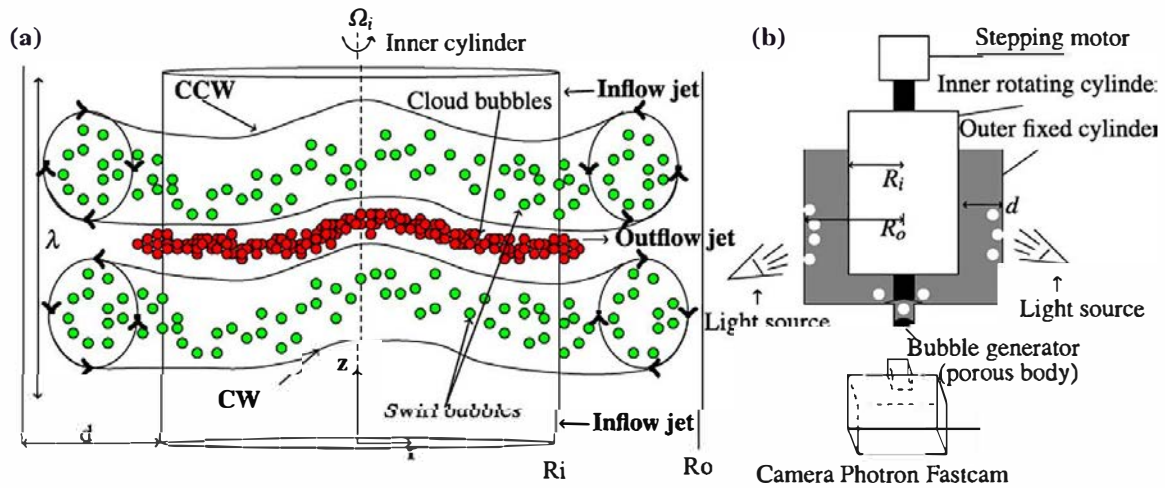Université de Brest, UBL, FRE CNRS 3744 IRDL, 29238 Brest, France

Fig. 1 a Triple capture mode [*red* (cloud bubbles) and *green* (swirl bubbles)]. b Experimental setup of vertical Taylor Couette flow system (*scale* does not fit with reality)

locations of bubbles in the crest and in the thought of the undulated vortices, which correspond to the low-pressure regions. These numerical results were confirmed by the experimental observations of Watamura et al. (2013), with the injection of microbubbles. By increasing the rotational speed of the inner cylinder in the weakly turbulent regimes, Chouippe et al. (2014) evidenced a capture of microbubbles in the herring-bone-like high-speed streaks near the inner cylinder.

Ndongo Fokoua et al. (2015) indicated that the drag acting on the inner cylinder wall can be increased or decreased, according to the preferential bubble location. In particular, bubbles accumulated in the outflow region near the inner cylinder play in favor of drag reduction, through an increase of the axial wavelength of Taylor vortices λ. Using a two-way-coupling method, Gao et al. (2015) demonstrated numerically that the wavelength of vortices is strongly influenced by the gas velocity. Sugiyama et al. (2008), as well as Spandan et al. (2016) investigated numerically the drag modification due to bubbles. Drag reduction is achieved through a destructuration or a weakening of the Taylor vortices. The study of bubbly drag reduction in Taylor–Couette flow was also extended to higher turbulent regimes by Van den Berg et al. (2005) and Van Gils et al. (2013). They highlighted the role played by the bubble deformability to enhance the drag reduction.

Moreover, with increasing gravity effect (Chouippe et al. 2014) or gas injection flux (Shiomi et al. 1993), the bubble arrangement can shift from a toroidal mode to a spiral mode. Interesting enough is that the maximum drag reduction is observed during the transition from the toroidal to the spiral regimes (Murai et al. 2008). Bubble distributions in a three-dimensional domain the consequence of two-way interaction between bubbles and liquid base flows, here TC flow. They have to be reflected by the influence of the drag reduction, and thus, knowing the time evolution of bubble distributions and velocity of accumulated bubbles is a key step towards understanding bubbly drag reduction processes. Individual bubble motions in bubble flow have been investigated (e.g., Murai et al. 2000), and the differences of behaviors between isolated bubbles and bubbles belonging to organized groups have also been discussed (e.g., Cheng et al. 2005). Furthermore, there are some reports performing the measurements of bubble distributions in a three-dimensional domain in bubbly conditions (e.g., Murai et al. 2001). However, general three-dimensional tracking for capturing bubble distributions is not applicable to the annular flow system in TC flow because of problems in optical configuration. Attempts to determine the local distribution in the radial-axial plane of bubbles and bubble velocity (Watamura et al. 2013; Ndongo Fokoua et al. 2015) based on individual bubble tracking techniques, however, cannot discriminate bubbles captured in the vortices (swirl bubbles, here after) from bubbles trapped in the outflow region near the inner cylinder (termed cloud bubbles, here after) in the triple capture mode (Fig. 1a) using their size. In fact, clouds can be superposed with swirl bubbles, as shown in Fig. 2a, which is a snapshot of bubble distributions in the triple capture mode. Moreover, the determination of azimuthal velocity of bubbles is crucial. Mehel et al. (2006) determined azimuthal velocity profiles of the gas phase in the vortex core by adopting intrusive dual fiber-optical probes, but this technique is not applicable in the near-wall region of the outflow, where bubbles are accumulated.

To our knowledge, the determination of azimuthal velocity of cloud bubble (bubbles which are accumulated near the inner cylinder) has not been addressed yet. The goal of this paper is to present an original

(a) Snapshot   **(b)** Bubble size distribution
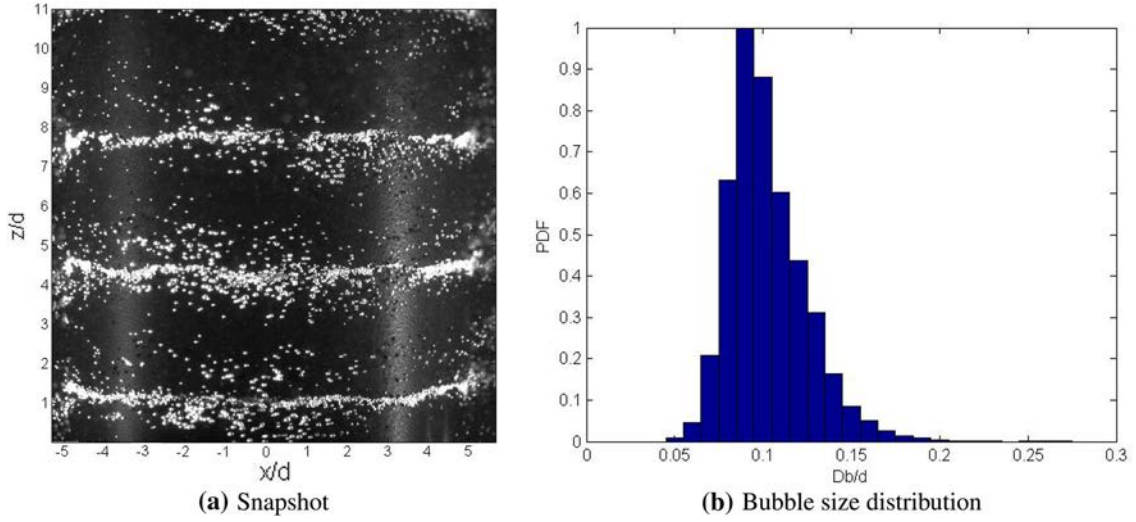
Fig. 2 a Snapshot of bubble distribution in toroidal regime ($Re \approx 1500, \alpha \approx 0.14$ %), and **b** corresponding bubble size distribution, where the mean value is $0.09d$ equivalent to $D_b \approx 1.08$ mm

experimental method to characterize the bubble distribution and bubble velocity in the azimuthal plane of a weakly turbulent bubbly TC flow, where bubbles are arranged as toroidal strings. In this paper, only one flow regime was tested. This flow regime is a compromise which leads to a triple capture in a toroidal arrangement, quite stable with regard to time. This configuration of the flow is achieved for a reduced range of Reynolds numbers and air-injection rates. When increasing the air-injection rate or decreasing the Reynolds number, there can be no bubble entrapment or there can be a coexistence between toroidal and spiral modes that induce a strong axial motion of the gas phase, which is out of applicability of the proposed method for the discrimination between cloud and swirl bubbles without a modification. The bubbly flow pattern is recorded by a high-speed video camera in the front view, as presented in Fig. 2a. The analysis is based on the development of a specific image processing that enables the separation of cloud and swirl bubbles. The temporal variations of azimuthal velocities of the cloud and swirl bubbles are obtained. The analysis is completed by the measurements of the preferential cloud bubble's position, the time variation of void fraction, and local volume fraction of gas phase. This paper is organized as follows: the next section is devoted to the description of the experimental device. The image processing for separating between the cloud and swirl bubbles is described in the third section. The fourth section is dedicated to results and discussions of the time variations of azimuthal velocities of the gas phase.

2 Experimental device and control parameters

The experiments were conducted in an apparatus of vertical TC flow system, as presented in Fig. 1b. The inner rotating cylinder is made of black resin with a radius $R_i = 60$ mm. The fixed outer cylinder is made of transparent acrylic resin with a radius $R_o = 72$ mm. The geometry is characterized by a radius ratio $\eta = R_i/R_o = 0.91$ and an aspect ratio $\Gamma = L/(R_o - R_i) = 20$, where L is the effective height of the liquid layer. A stepper motor with rotational speed Ω_i that can be varied from 0 to 300 rpm is mounted on the shaft connected to the inner cylinder. 10 cSt silicone oil is used as a working fluid; physical properties of the fluid are summarized in Table 1. The bubbles generator, located below the annulus, is made of porous material, which makes possible to inject air bubbles of average size D_b approximately ten times smaller than the gap width $d = (R_o - R_i) = 12$ mm. The gas flow rate can be varied from $Q_g = [2.5 - 16.7] \times 10^{-7} \text{m}^3 \text{ s}^{-1}$ and controlled using a gas flow rate meter with accuracy $\delta Q_g = \pm 1.67 \times 10^{-8} \text{ m}^3 \text{ s}^{-1}$. The bubbly TC flow is driven by the Reynolds number, which compares inertia and viscous effects of the liquid phase and is defined as $Re = 2\pi R_i \Omega_i d/\nu$ (ν is kinematic viscosity), and the global void fraction for the gas phase:

$$\alpha = \frac{Qg}{2\pi R_i d V_b}, \ V_b = \sqrt{\frac{4}{3} g \frac{D_b}{C_d}}, \tag{1}$$

Table 1 Specifications of dimensions of the apparatus, physical properties of the test fluid, 10 cSt silicon oil, and setting parameters

Apparatus		
Inner cylinder diameter	R_i	60 mm
Outer cylinder diameter	R_o	72 mm
Gap	d	12 mm
Height of the liquid column	L	240 mm
Physical properties of the fluid		
Density	ρ	930 kg/m^3
Surface tension	σ	20.1×10^{-3} N/m
Kinematic viscosity	v	1.004×10^{-5} m^2/s
Mean bubble diameter	D_b	1.08 mm
Angular velocity	Ω_i	3.33 tr/s
Velocity	$V_i \quad 2\pi R_i \Omega_i$	1.26 m/s
Gas flow rate	Q_g	4.17×10^{-7} m^3 s^{-1}
Reynold number	Re	1500
Global void fraction	α	0.14 %
Bubbles rising velocity	V_b	0.065 m/s
Drag coefficient (Mei et al. 1994)	C_d	3.26

where V_b is terminal rising velocity of the bubbles in still liquid. With C_d, the drag coefficient of bubbles estimated from Mei et al. (1994):

$$C_d = \frac{16}{Re_B}\left\{1 + \left[\frac{8}{Re_B} + \frac{1}{2}(1 + 3.315 Re_B{}^{0.5})\right]^{-1}\right\}, \tag{2}$$
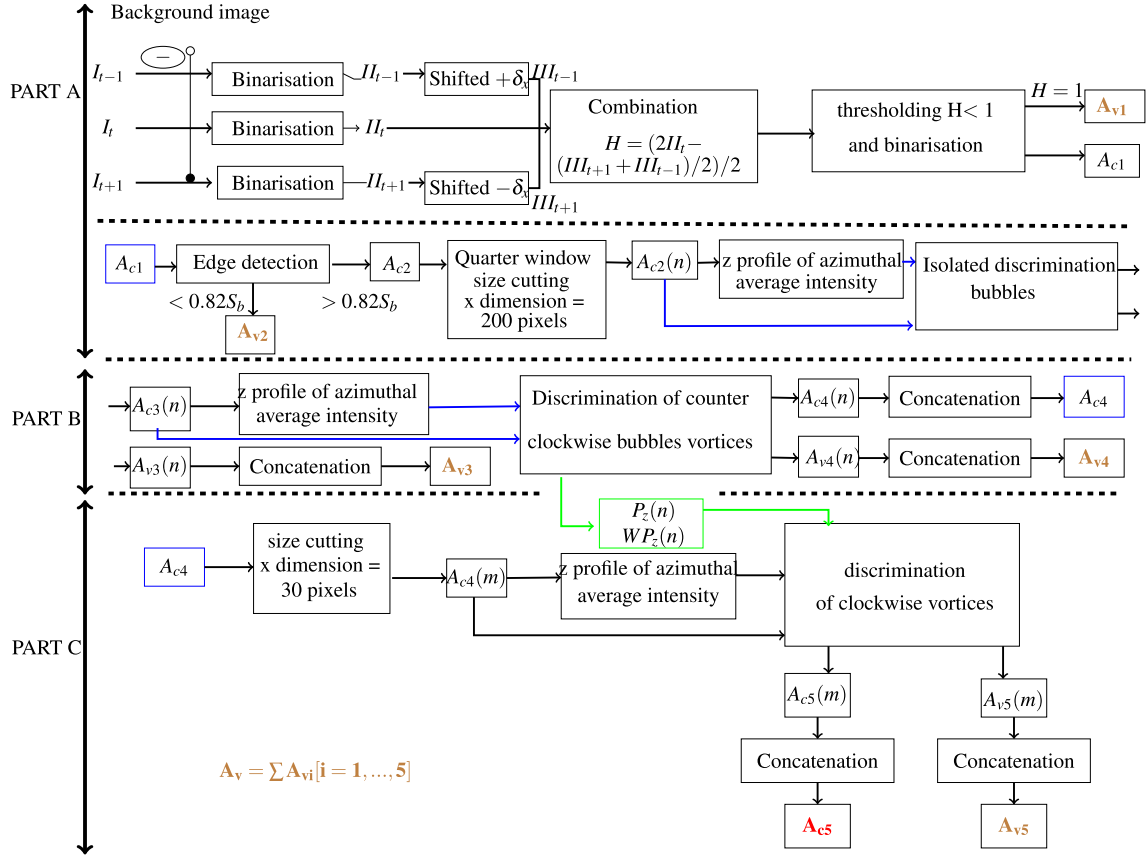
with $Re_B = (V_b D_b)/v$ being the bubble Reynolds number.

The observed flow regimes are recorded using a high-speed video camera, Photron Fastcam-Max, with a Nitro-Nikkor lens of 105 mm F/2.8. To obtain a good contrast in the image (c.f. Fig. 2a), two light projectors were used at the sides of TC flow setup, as presented in Fig. 1b. The scale factor of images was 0.1289 mm/pixel, and the shutter speed of the camera was set at 1/3000 s. The field of view was 132 mm in the azimuthal direction x, centred on the cylinder axis and 132 mm in the axial direction z, with a scale factor of 129 μm/pixel. We focused on the toroidal regime obtained for the following control parameters, $Re = 1500$, $Q_g = 4.17 \times 10^{-7}$ m^3 s^{-1} (equivalent to $\alpha = 0.14$ %). The experimental conditions are summarized in Table 1. For this Re number, which is 16 times the critical Reynolds number for the onset of Taylor vortices (primary instability), the flow is considered weakly turbulent. Front view recorded images depict the presence of cloud and swirl bubbles, periodically arranged in the axial direction with an axial wavelength $\lambda = 3.18d$. The corresponding probability density distribution of bubble size is presented in Fig. 2b. The equivalent diameter of the bubbles was determined based on a reduced image in the x direction (width $x = \pm d$ on both the sides of the rotation axis) and by applying a procedure of edges detection with a criterium of sphericity. This procedure limits the contribution of curvature-induced distortion to the bubbles size distribution. The next subsection is devoted to explaining the image-processing method through considering the characteristics of the cloud and swirl bubbles.

3 Image processing for recognising cloud and swirl bubbles

For the experimental conditions, the field of view highlights three bubble patterns, each of them being composed of a triple capture (Fig. 2a). As described in Fig. 1a, bubbles are trapped in CCW, CW vortices, and in the outflow region. For this typical bubble arrangement, a simple image processing based on the location of bubbles does not work to separate the cloud bubbles from swirl bubbles. Indeed, it is particularly difficult to separate accumulated bubbles in the counter-clockwise vortex from cloud bubbles, because they are located quite near each other, as shown in a snapshot of Fig. 2a. For this purpose, a specific image-processing method was developed.

The image-processing program is composed of three main parts: Part A is devoted to discriminating isolated bubbles in vortices. Part B is focused on the discrimination of the bubbles accumulated in counter-clockwise vortices, whereas part C aims at discriminating the accumulated bubbles in the clockwise vortices. A general sketch of the separation algorithm is presented in Fig. 3. Matrices A_{vi} denote binarized images of swirl bubbles extracted from the original binarized image I_t at different steps i of the processing.

Background image

PART A

I_{t-1} → Binarisation → II_{t-1} → Shifted $+\delta_x$ → III_{t-1}

I_t → Binarisation → II_t

I_{t+1} → Binarisation → II_{t+1} → Shifted $-\delta_x$ → III_{t+1}

Combination
$H = (2II_t - (III_{t+1} + III_{t-1})/2)/2$

thresholding H< 1 and binarisation

$H = 1$ → A_{v1}

A_{c1}

A_{c1} → Edge detection → A_{c2} → Quarter window size cutting x dimension = 200 pixels → $A_{c2}(n)$ → z profile of azimuthal average intensity → Isolated discrimination bubbles

$< 0.82S_b$ ↓ $> 0.82S_b$

A_{v2}

PART B

$A_{c3}(n)$ → z profile of azimuthal average intensity → Discrimination of counter clockwise bubbles vortices → $A_{c4}(n)$ → Concatenation → A_{c4}

$A_{v3}(n)$ → Concatenation → A_{v3} → $A_{v4}(n)$ → Concatenation → A_{v4}

$P_z(n)$
$WP_z(n)$

PART C

A_{c4} → size cutting x dimension = 30 pixels → $A_{c4}(m)$ → z profile of azimuthal average intensity → discrimination of clockwise vortices

$A_{c5}(m)$ $A_{v5}(m)$

Concatenation Concatenation

A_{c5} A_{v5}

$A_v = \sum A_{vi}[i = 1, ..., 5]$

Fig. 3 General sketch of the algorithm used for to swirl and cloud bubbles discrimination

The final image of swirl bubbles A_v is obtained from summation of A_{vi}. Matrices A_{ci} denote binarized images of the remaining bubbles after removing swirl bubbles at different steps. At the end of the processing, A_{c5} is the final image of cloud bubbles. The different steps will now be detailed and illustrated by displaying some snapshots in Fig. 4.

, I_t, is displayed in Fig. 4a. For all snapshots, after removing the background, a 2D filtering (Oppenheim et al. 1989 with 0.5 as parameter) was applied, where the function filters a data sequence using a digital filter which is a 2D convolution operator using a 2D Finite-Impulse Response (FIR) filter. The snapshots were then binarized, based on a single threshold determined by the Otsu method (Otsu 1979) (see an example of binarized images II_t in Fig. 4b). The bubble size can be deduced from binarized images after applying an edge detection procedure and a criterion of sphericity in shape. Mean bubble diameter D_b is thus obtained as the average value, here $D_b = 1.08$ mm. Considering that accumulated bubbles are organized as apparent large gas structures that keep similarity in shape at consecutive time steps, the correlation in x direction was calculated between binarized image at time t, and $t-1$, after applying an edge detection procedure and saving the biggest structures (equivalent diameter $> 96D_b$). This procedure allowed the determination of the most probable displacement δx of apparent large gas structures between two time steps. Matrix H represents local correlation deduced from three time-step sequential images taken at time t, $t-1$ shifted with $+\delta x(III_{t\ 1})$ and $t+1$ shifted with $\delta x(III_{t+1})$ as :

$$H = \left(2II_t - \frac{III_{t+1} + III_{t\ 1}}{2}\right)/2. \tag{3}$$

H is a gray-level matrix taking values, $H = 1, 0.5$ or 0.75; an example is given in Fig. 4c. $H = 1$ is representative of minimum correlation between these images. Pixel values of H equal to 1 are attributed to isolated bubbles in vortices and memorized into a binarized matrix A_{v1} (Fig. 4d). Otherwise, pixel values of H less than 1 are attributed to accumulated bubbles and memorized into a binarized image A_{c1} (Fig. 4e). An edge detection procedure was then applied on A_{c1} to identify possible isolated bubbles that were not
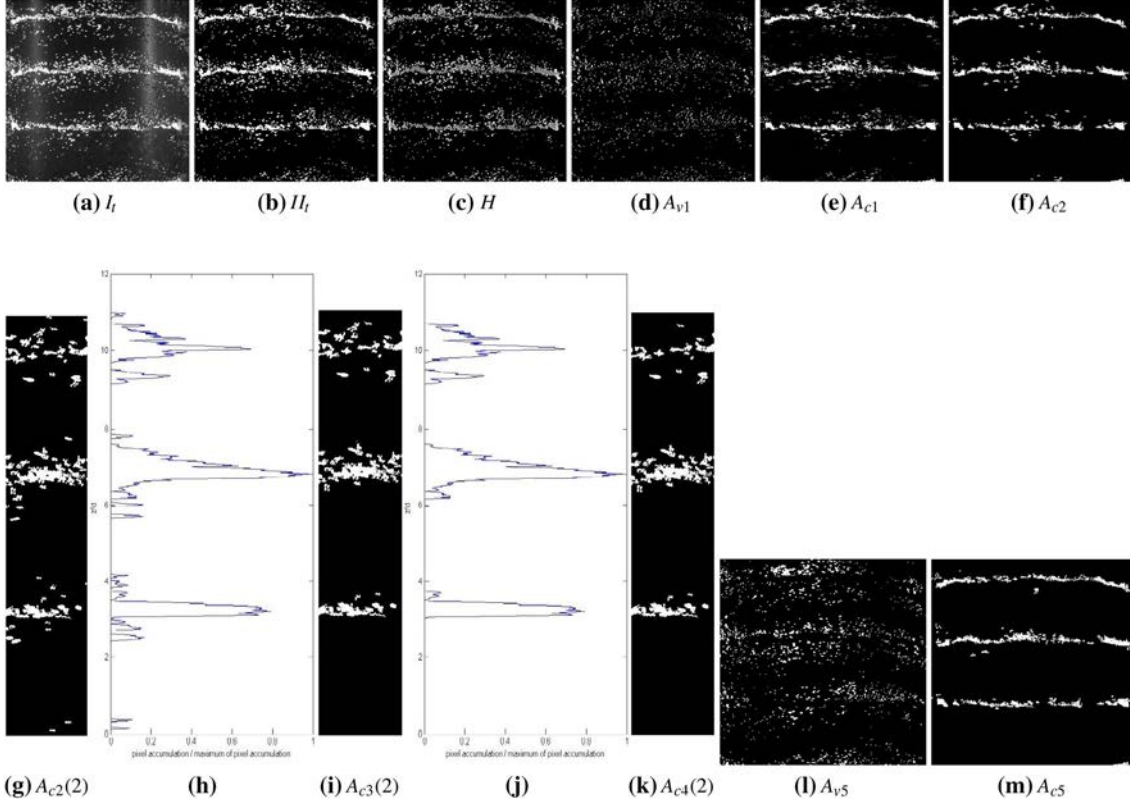
Fig. 4 **a** Raw image at a time step t (I_t), **b** binalized image with removing background image (II_t) of I_t. **c** Correlation of bubble distribution patterns between three sequential images (H), binalized images of **d** dispersed bubbles in vortices (A_{c2}) and **e** organized bubbles (A_{c1}), **f** results of eliminating small bubble groups, **g** extracted images of A_{c2}, $A_{c2}(2)$ and x average of $A_{c2}(2)$, **h** results of eliminating isolated bubbles, $A_{c3}(2)$, and **j** its x average, **k** results of removing bubbles accumulated in the counter clockwise vortices (A_{c4}), binalized images of **l** swirl bubbles (A_{v5}) and **m** cloud bubbles (A_{c5}) as results of image processing

discriminated by the previous procedure. Pixels in the objects, whose area being smaller than $S_b = 0.82\pi D_b^2/4$, were attributed to isolated bubbles and memorized into A_{v2}, where the factor 0.82 was empirically determined according to H matrices results. A_{c2} displayed in Fig. 4f is the result of the processing of the remaining bubbles, after removing non-correlated gas structures in time and removing dispersed bubbles with small area.

As bubbles trapped in vortices and clouds are arranged as strings in the azimuthal direction (x direction on the images), the next steps of the processing are based on the identification of bubble preferential location in the axial direction (z direction on the images). The azimuthal waviness shifts the axial location of accumulated bubbles according to x direction. Therefore, to minimize this effect, the images A_{c2} are divided into four pieces in the x direction as $A_{c2}(n)$, ($n = 1$–4). Normalized profiles of x averaged intensity on $A_{c2}(2)$ (Fig. 4g) were plotted with regard to z direction (Fig. 4h). The profiles exhibit several peaks, each of them being characterized by a maximum intensity and a width in the z direction. Isolated bubbles, organized as strings, tend to have narrower peak with smaller intensity. Thus, based on the average size of the bubbles, a criterion was applied on these two parameters to identify peaks that belong to the remaining isolated bubbles. Pixels on $A_{c2}(n)$ at the z location of these peaks were then considered as being part of isolated bubbles and recorded into matrix $A_{v3}(n)$. $A_{c3}(n)$ displayed in Fig. 4i is the result of this procedure after removing isolated bubbles. The next step of the processing aims at discriminating bubbles accumulated in the counter-clockwise vortices which were expected to be located above the cloud bubbles. For this situation, the profiles of x averaged intensity based on $A_{c3}(n)$ (as shown in Fig. 4j) for the upper string can evidence large peaks in z direction that results from the combination of two prominent peaks. Several criteria were applied, such as the width of the global peak, the distance between two maxima of intensity, and the minimum intensity between two maxima. The z location of the minimum intensity was used to discriminate bubbles: indeed, the upper part of $A_{c3}(n)$ was then considered as part of bubbles in counter-clockwise vortices and recorded in $A_{v4}(n)$, whereas the lower part was recorded in $A_{c4}(n)$ (see Fig. 4k). The

z location of the bottom peak $P_z(n)$ was considered as the most probable position of the cloud bubbles; the width of the bottom peak $WP_z(n)$, as well as $P_z(n)$ are utilized in the next step. A_{c4} is then composed of cloud bubbles and possible remaining bubbles that are accumulated in clockwise vortices, which were expected to be located under the cloud bubbles.

As fewer bubbles are trapped by the CW vortices than by the CCW vortices, the clockwise swirl bubbles were drowned in the intensity peak of cloud bubbles at the previous step. Thus, the discrimination of bubbles accumulated in the clockwise vortices requires a refinement of x averaged intensity analysis. For this purpose, we reduced the size of A_{c4} in the x direction [$A_{c4}(m)$ is defined for a width in x direction of 30 pixels, i.e., $3.75D_b$]. Peaks of $A_{c4}(m)$ located under $P_z(n)$, taking into account $W_{P_z}(n)$, are attributed to bubbles in clockwise vortices, associated pixels are then recorded into $A_{v5}(m)$, and otherwise, pixels are attributed to cloud bubbles and saved into $A_{c5}(m)$. The final images, A_v (Fig. 4l) and A_{c5} (Fig. 4m), are the results of the global discrimination procedure at time t for swirl bubbles and cloud bubbles, respectively. The maximum of the correlation in x direction between images A_v (respectively A_{c5} at time t and $t + 1$) was used for the determination of averaged azimuthal velocity of the bubbles V_θ at time t in vortices (and clouds respectively). The image-processing method developed here is limited to bubbles arrangements for which the axial motion of the bubbles induced by the buoyancy effect (regardless of the waviness motion) is characterized by a much smaller time constant than the one that characterizes the azimuthal waviness. Otherwise, it is not possible to distinguish peaks in the axial direction of the x-averaged intensity, which are used to discriminate swirl from cloud bubbles. This situation can be encountered when increasing the air-injection rate or decreasing the Reynolds number.

4 Results and discussions

From A_v (respectively A_{c5}), the intensity I_z was extracted at $x = 0$ along a line in the axial direction z. The stored lines at regular intervals of time were stacked together to provide space-time diagrams I_{zt}. The space–time diagram of toroidal regime is presented in Fig. 5, where bubbles in the vortices (green) and cloud bubbles (red) are displayed in different colors. The axial position and time are normalized by the gap width d and the rotational period of the inner cylinder $T_i = 1/\Omega_i$, respectively.

The space–time diagram in Fig. 5 shows wavy undulations of the bubble strings and highlights elevation in time of the waviness. Yoshida et al. (2009) has similar results before a transition between a toroidal mode to a spiral mode, the author explained that the cluster move upward gradually driven by the buoyancy effect. However, in our case, a transition from a toroidal to spiral modes has not occurred. This particular regime which has not been evidenced for the toroidal mode in the previous works is called elevated toroidal mode (ETM). The averaged rising velocity W_b can be determined by correlation in the axial direction of the spatial temporal diagram (taking into account swirl and cloud bubbles). For the conditions of this study, the rising velocity is equal to $W_b = 0.026V_b$. In fact, all the bubble strings are moving upward, each time the top one disappeared at the free surface, and a new one was generated at the bottom. At $t/T_i = 35$ an ejection is observed from the bottom to the top, this ejection has a similar behavior as an unique spiral which enables the release of individual bubbles from a bubble string to a another one located upper but without destroying the axial toroidal arrangement of the flow.

The Fast Fourier Transformation (FFT) was used to measure the frequency of wavy undulations of all the kinds of bubbles. The mean power spectrum exhibits a frequency of the toroidal regime equal to
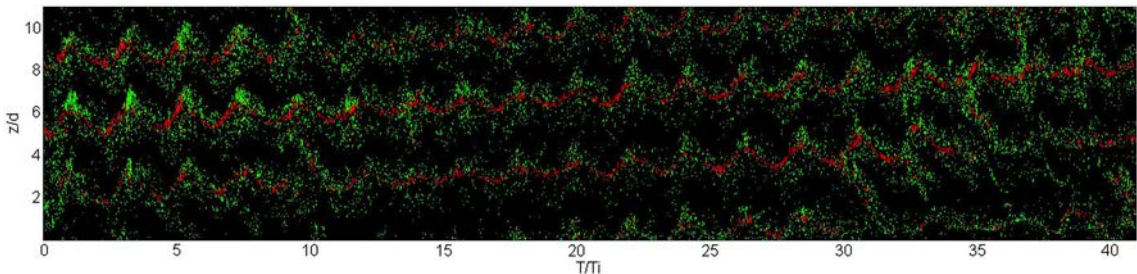
Fig. 5 Space time diagram of advecting bubbles in elevated toroidal mode (ETM) extracted at r 0 for Re 1500 and α 0.14 % (*green* swirl bubbles and *red* cloud bubbles)
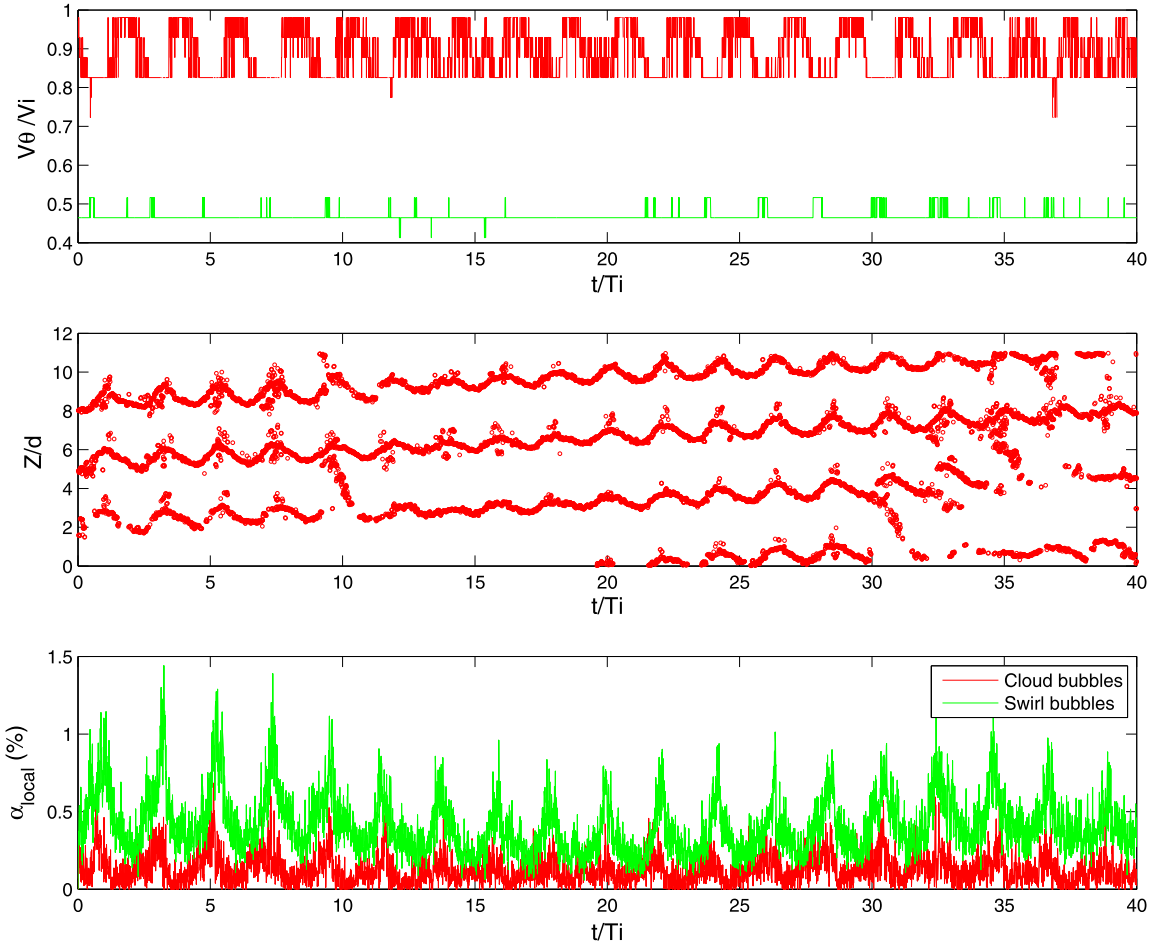
Fig. 6 Properties of cloud and swirl bubbles as a function of time ($Re \simeq 1500$, $\alpha \simeq 0.14$ %); **a** azimuthal velocity of bubbles, V_θ, **b** preferential axial location of cloud bubbles, and **c** apparent local void fraction, α_{local}

$f = 0.47/T_i$. By the observation of the toroidal regime, the azimuthal wave number is equal to $k_\theta = 1$. Thus, the phase velocity of the azimuthal waviness is $c_\theta = 2\pi f R_i/k_\theta \approx 0.47V_i$.

The maximum of the correlation in x direction between images A_v (respectively A_{c5}) at time t and $t+1$ was used for the determination of averaged azimuthal velocity of the bubbles V_θ at time t in vortices (and clouds respectively). The evolution of V_θ normalized by the azimuthal velocity of the inner cylinder V_i, is plotted in Fig. 6a as a function of the normalized time. The azimuthal velocity of swirl bubbles is almost constant, $V_\theta \simeq 0.47V_i$. Mehel et al. (2006) measured in the core of the vortices a value of the azimuthal velocity of the gas phase ($V_\theta \simeq 0.44V_i$), which can be attributed to the azimuthal velocity of swirl bubbles. This value is close to what we obtained in our experiment. It is in agreement with the azimuthal velocity of the liquid phase, expected in the middle of the gap. Indeed, as pointed out by numerical simulations of Climent et al. (2007) and measurements of Mehel et al. (2006), the drift velocity in the azimuthal direction between liquid and swirl bubbles is expected to be small. The phase velocity of azimuthal wavy motion (c_θ) is equal to the azimuthal velocity of swirl bubbles. This means that the wavy undulation of the gas structure is induced by the bubbles trapping inside the vortices, i.e., swirl bubbles. For cloud bubbles, a higher azimuthal velocity is obtained by image processing ($V_\theta = 0.82V_i$ to $0.98V_i$). This higher velocity can be explained by position of the cloud bubbles located near the rotating inner cylinder. The cloud bubbles velocity varies periodically with time (Fig. 6a). To explain this periodicity, it is convenient to introduce Fig. 6b which gives the most probable axial position of cloud bubbles with time extracted from the maximal intensity peaks (P_z) in A_{c4}. Along the waviness, the velocity of cloud bubbles increases at the end of the trough and it decreases at the top of the crest. The velocity tends to be constant otherwise. Furthermore, physical information that can be extracted after the image processing is the equivalent void fraction plotted

with time for swirl bubbles and clouds separately (Fig. 6c). To catch the temporal evolution of the void fraction due to the waviness, the analysis was performed on images A_v (respectively A_{c5}), whose size being reduced to $x = \pm 0.6 D_b$. Assuming that bubbles are spherical, apparent local void fraction is calculated using the following formula:

$$\alpha_{\text{local}} = \frac{S_{\text{bubbles}}}{A} \frac{<D_b>2/3}{d},\tag{4}$$

where S_{bubbles} is the total area occupied by bubbles, and A is the area of reduced images. Figure 6c highlights that bubbles are preferentially trapped at the top of the crests of the wavy motion, in agreement with a decrease of the azimuthal velocity of cloud bubbles. Referring to Climent et al. (2007), the maximum of α_{local} corresponds to the local minimum of pressure at the crests. An axial transfer of bubbles was also observed. This transfer preferentially occurs at the crest of the wavy motion; it is due to the existence of an axial flow that connects the vortices.

5 Conclusion

We experimentally investigated the structure of the gas phase in a bubbly Taylor–Couette flow at $Re = 1500$ and $\alpha = 0.14$ %. For these conditions, bubbles are arranged as toroidal strings, periodically spaced in the axial direction, and submitted to an azimuthal wavy motion. Bubbles are accumulated in clouds near the inner cylinder in outflow jets (cloud bubbles) and in Taylor vortices (swirl bubbles). This paper first provides the characterization of bubbles accumulated in the clouds. To achieve this, a high-speed camera was used to record this flow in the vertical plane. A specific image-processing algorithm was developed to discriminate cloud bubbles from swirl bubbles according to the characteristics of the bubbles behaviors. This method delivers information about the time evolutions of location, azimuthal velocity, and equivalent void fraction of swirl and cloud bubbles separately. The velocity of swirl bubbles ($0.47V_i$) is in agreement with the phase velocity of the observed azimuthal wave, letting us suppose that the waviness is clearly driven by the bubble's entrapment in vortices. The azimuthal velocity of cloud bubbles oscillates from 0.82 to $0.98V_i$, depending on their location, following the azimuthal wave. Based on the analysis of apparent local void fraction, velocity, and location, cloud bubbles are accumulated at the crest, where the azimuthal velocity of cloud bubbles decreases. This brings bubbles to be release from the cloud to the connecting upper vortices and induces an axial flux of the gas. An elevation with time of the toroidal strings is also observed. This mechanism of releasing bubbles, which is associated with a drift velocity of the bubbles at the inner cylinder wall in comparison with the liquid, may be partly responsible for bubbly drag reduction observed in bubbly Taylor–Couette flow. The specific image-processing developed in this paper has a universality for toroidal mode and elevated toroidal mode characterized by moderate air-injection rates. For the spiral mode, a correction should be applied, taking into account the inclination of the bubble strings in the vertical-azimuthal plane induced by an important axial velocity of the gas phase.

References

Cheng W, Murai Y, Sasaki T, Yamamoto F (2005) Bubble velocity measurement with recursive cross correlation PIV technique. Flow Meas Instr 16:35 46

Chouippe A, Climent E, Legendre D, Gabillet C (2014) Numerical simulation of bubble dispersion in turbulent Taylor Couette flow. Phys Fluids Am Inst Phys 26(4):043304:1 22

Climent E, Simmonnet M, Magnaudet J (2007) Preferencial accumulation of bubbles in Couette Taylor flow patterns. Phys Fluids 19:083301

Fokoua GN, Gabillet C, Aubert A, Colin C (2015) Effect of bubbles arrangement on the viscous torque in bubbly Taylor Couette flow. Phys Fluids 27:034105 1 034105 34

Gao X, Kong B, Vigil RD (2015) CFD investigation of bubble effects on Taylor Couette flow patterns in the weakly turbulent vortex regime. Chem Eng J 270:508 518

Kumagai I, Takahashi Y, Murai Y (2015) Power saving device for air bubble generation using a hydrofoil to reduce ship drag: theory, experiments, and application to ships. Ocean Eng 95:183 194

Mehel A, Gabillet G, Djeridi H (2006) Bubble effect on the structures of weakly turbulent Couette Taylor flow. J Fluids Eng 128(4). doi:10.1115/1.2201641

Mei R, Klausner J, Lawrence C (1994) A note on the history force on a spherical bubble at finite Reynolds number. Phys Fluids 6:418 420

Murai Y, Matsumoro Y, Yamamoto F (2001) Three dimensional measurement of void fraction in a bubble plume using statistic stereoscopic image processing. Exp Fluids 30:11 21

Murai Y, Matsumoto Y, Yamamoto F (2000) Qualitative and quantitative flow visualization of bubble motions in a plane bubble plume. J Vis 3:27 35

Murai Y, Oiwa H, Takeda Y (2008) Frictional drag reduction in bubbly Couette Taylor flow. Phys Fluids 20:034101

Oppenheim A, Schafer RW, Buck JR (1989) Discrete time signal processing. Prentice Hall, Englewood Cliffs, pp 311 312

Otsu N (1979) Threshold selection method from Gray level histograms. IEEE Trans Syst Man Cybern 9(1):62 66

Shiomi Y, Kutsuna H, Akagawa K, Ozawa M (1993) Two phase flow in an annulus with a rotating inner cylinder (flow pattern in bubbly flow region). Nuc Eng Des 141(1E):27 34

Spandan V, Ostilla Mnico R, Verzicco R, Lohse D (2016) Drag reduction in numerical two phase Taylor Couette turbulence using an Euler Lagrange approach. J Fluid Mech 798:411 435

Sugiyama K, Calzavarini E, Lohse D (2008) Microbubbly drag reduction in Taylor Couette flow in the wavy vortex regime. J Fluid Mech 608:21 24

Van Gils DPM, Guzman DN, Sun C (2013) The importance of bubble deformability for strong drag reduction in bubbly turbulent Taylor Couette flow. J Fluid Mech 722:317 347

Van den Berg TH, Luther S, Lathrop DP, Lohse D (2005) Drag reduction in Bubbly Taylor Couette turbulence. Phys Rev Lett 94:044501

Watamura T, Tasaka Y, Murai Y (2013) Intensified and attenuated waves in a microbubble Taylor Couette flow. Phys Fluids 25:054107

Yoshida K, Tasaka Y, Murai Y, Takeda T (2009) Mode transition in bubbly Taylor Couette flow measured by PTV. J Phys Conf Ser 147:012013